Imaging radar for navigation and surveillance on an autonomous unmanned ground vehicle capable of detecting obstacles obscured by vegetation

Daniel Gusland, Børge Torvik, Erlend Finden, Fredrik Gulbrandsen and Ragnar Smestad
Norwegian Defence Research Establishment (FFI)
Kjeller, Norway
Email: daniel.gusland@ffi.no, borge.torvik@ffi.no, ragnar.smestad@ffi.no, fredrik.gulbrandsen@ffi.no

***Abstract*—The Norwegian Defence Research Establishment (FFI), has developed a multi purpose radar demonstrator for Intelligence, Surveillance and Reconnaissance (ISR) on the Off-road Light Autonomous Vehicle (OLAV) platform. The radar is designed to aid OLAV in navigation, detection and classification. Operating in off-road environments is a considerable challenge for autonomous vehicles, especially in the presence of vegetation. While existing perception sensors such as cameras and LIght Detection And Ranging (LiDAR) work well in clear weather and areas without vegetation, they are impaired by rain, fog, smoke and vegetation. This paper presents the development of the Multiple Usage Radar - S-band (MURA-S), developed to aid the autonomous platforms in challenging conditions. Initial considerations and frequency selection for the radar is presented in addition to a detailed explanation of the antenna configuration and the utilization of time-domain multiplexed Multiple-Input Multiple-Output (MIMO) techniques to increase the cross-range resolution of the radar. Preliminary experimental results for detecting obstacles obscured by vegetation are presented and compared with obstacle maps created by the LiDAR, showing that the radar enhances the capabilities of the perception system.**

***Index Terms*—Radar, MIMO, obstacle detection, Unmanned autonomous vehicles**

I. Introduction

FFI has developed an autonomous off-road vehicle called OLAV. OLAV's primary mission is to navigate to a specific location and observe using on board sensors [1]. This publication covers the development of a radar sensor for autonomous platforms such as OLAV. The radar should increase the platform capacity for perception, detection and surveillance. It is hypothesized that the radar should aid the perception system in scenarios with excessive fog or dust and in situations where vegetation may hide obstacles. Radars have successfully been used for perception on autonomous vehicles in the presence of fog and dust [2], [3]. Attenuation of microwaves through vegetation generally increases with frequency [4], and the effects on obstacle classification can be summarized as: attenuation, backscatter, phase variation and depolarization [5]. Experimental systems with low center frequencies have demonstrated obstacle detection through foliage. The U.S. Army Research Laboratory (ARL) has developed a forward-looking ground penetrating radar sensor called SIRE [6], later SAFIRE, that has been used for autonomous navigation and detection of obstacles through vegetation. The Korean agency for defense development has developed a UWB (Ultra Wideband) forward imaging radar for an unmanned ground vehicle [7], somewhat similar to SIRE, with the goal of detecting obstacles through vegetation. This paper presents the development of the MURA-S, capable of detecting obstacles obscured by vegetation and performing surveillance tasks such as detection and classification of UAS (Unmanned Aerial System) and personnel.

II. The MURA-S radar system

The defining design goal of MURA-S was making a multi purpose system. However, the radar should solve specific tasks that put limitations on system parameters, such as obstacle detection through vegetation and UAS detection. To enable the system to image a scene from short range a Frequency-Modulated Continuous Wave (FMCW) architecture was selected. To increase classification capabilities for UAS [8] and terrain [9] the system was designed to be polarimetric. The antenna is configured as an array and all the receiving channels are digitized to give the system flexibility with regards to processing techniques.

A. Carrier frequency selection

Selecting the carrier frequency for a multi purpose radar is a trade-off of several traits. As previously mentioned the attenuation of microwaves through vegetation generally increases with frequency. However, lower frequencies result in lower cross-range resolution compared to antenna size. In general there is also less available bandwidth in the lower frequency radar bands, resulting in lower range-resolution. Reports of attenuation through vegetation are highly variable, likely due to variations in water content and volume density. To quantify the attenuation in relevant cases, the attenuation was measured using a VNA (Vector Network Analyzer), polarimetric wide-band antennas and a trihedral corner reflector placed behind a patch of vegetation. The vegetation, as shown in Fig. 1, was a mix of grass, broadleaf and shrubs and fairly moist. The

experiment was repeated over several patches and the results were averaged.

Fig. 1: Image of one vegetation patch used for the attenuation measurements.

Fig. 2 shows average attenuation for multiple incidence angles as dB/m for each polarization as a function of frequency. Analyzing the results reveal that the attenuation below 4 GHz for horizontal polarization is quite low. The attenuation increases rapidly from 4–8 GHz and increases at a lower rate beyond 8 GHz.

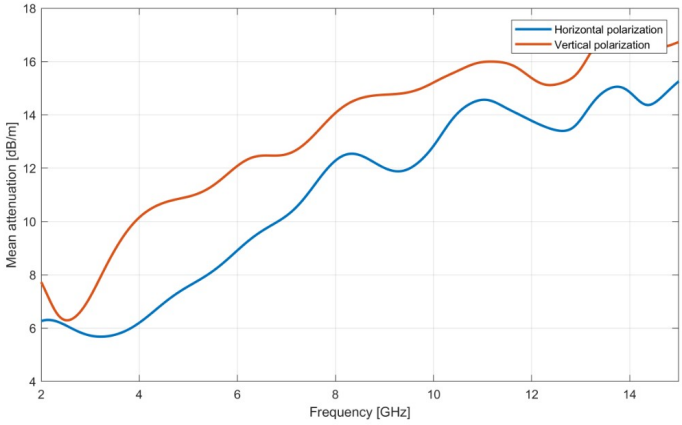

Fig. 2: Horizontal and vertical attenuation for the two-way measurement setup averaged over all heights.

When evaluating the frequencies, the contrast between relevant obstacles and vegetation clutter is of critical importance. The contrast can be defined as the maximum reflected power of the resolution cell containing obstacle compared to the maximum of the vegetation surrounding it. This measure incorporates both the target response, vegetation attenuation and vegetation backscatter. Using a VNA, Synthetic Aperture Radar (SAR)-rail system and time-domain backprojection, the contrast between several relevant obstacles and vegetated background was measured at frequencies ranging from 3 to 14 GHz. An image of the setup and the measurement scene is shown in Fig. 3. The VNA sweeps from 2.5–14.5 GHz. This is used to generate backprojected images using 1 GHz bandwidth with center frequencies from 3–14 GHz. The contrast from an occluded tree stub is presented in Fig. 4. The best contrast is found between 3–8 GHz for this obstacle. Note that the backscatter from vegetation is higher than the target response in this experiment at frequencies above 11 GHz. To achieve an acceptable contrast and comply with frequency regulations, the system was designed with a center frequency of 3.2 GHz.

Fig. 3: Image of the measurement setup for target contrast measurements, the targets are hidden in vegetation.

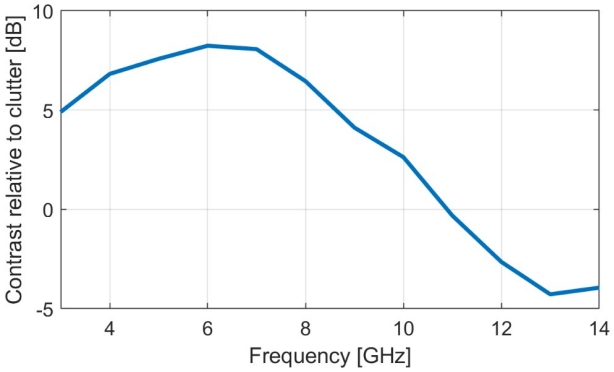

Fig. 4: Target contrast of a tree stub compared to surrounding vegetation as a function of frequency using horizontal polarization.

B. Range and cross-range resolution

Any mapping system would benefit from a high resolution in range and cross-range. The system also needed to fit within the confines of the test vehicle platform OLAV. It is desirable to have range and cross-range resolution close to or smaller

than the size of the relevant obstacles. The range resolution of an FMCW system is defined as:

$$\rho_r = \frac{cK_r}{2B} \tag{1}$$

Where c is the speed of light, B is the bandwidth of the chirp and K_r is the excess bandwidth scaling factor to compensate for the broadening induced by aperture weighting. Utilizing the full available bandwidth of 400 MHz gives us a range resolution of 0.56 m when applying a Hanning window function.

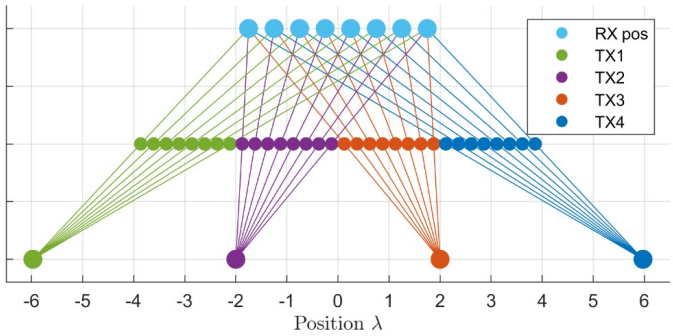

Fig. 5: Illustration showing the receive array, the optimal transmit positions and their approximate phase centers as described by Charvat [10].

To achieve a satisfactory cross-range resolution using a reasonable number of channels, a time-domain separated MIMO technique was employed. When the transmit and receive antennas are close to each other, relative to the range to the target, the equivalent phase center is mid-way between the transmit and receive pair [10]. This technique has, albeit with different antenna configurations, been utilized by several other systems [6], [7], [11]. By utilizing this technique an 8-element receive array was coupled with four transmit antennas, achieving 32 equally spaced phase centers providing a cross-range resolution that is four times higher than using just one transmit antenna.

Designers of systems utilizing similar antenna configurations have reported elevated sidelobes, resulting in an increased "noise floor" [7] [12]. Their designs have the Tx antennas at the same cross-range position as the outer most Rx antennas. To investigate this, the Point Spread Response (PSR) at 10 meters was simulated for three antenna configurations; one centered Tx antenna, two Tx antennas at the same cross-range position as the outer most Rx antennas and lastly two Tx antennas positioned a quarter wavelength outside of the outer most Rx antennas. Fig. 6 shows the simulated cross-range PSR of these configurations when using time-domain backprojection and applying a Hanning window across the array prior to imaging. The first observation is the cross-range resolution improvement achieved by using two transmitters. It is also evident that the PSR of the second configuration settles at a mere -19 dB, whereas the PSR of the corrected configuration settles at approximately -46 dB. Following the logic that the equivalent phase center is mid-way between a Tx/Rx pair, having the Tx antennas in line with the outer most Rx antennas effectively samples the antenna center twice, resulting in uneven sampling. The correct position for the transmit antennas was found to be $\frac{\lambda}{4}$ and $4\lambda + \frac{\lambda}{4}$ outside the outer most receive element as shown in Fig. 5 giving us an imaging geometry as shown in Fig. 7 for four Tx antennas.

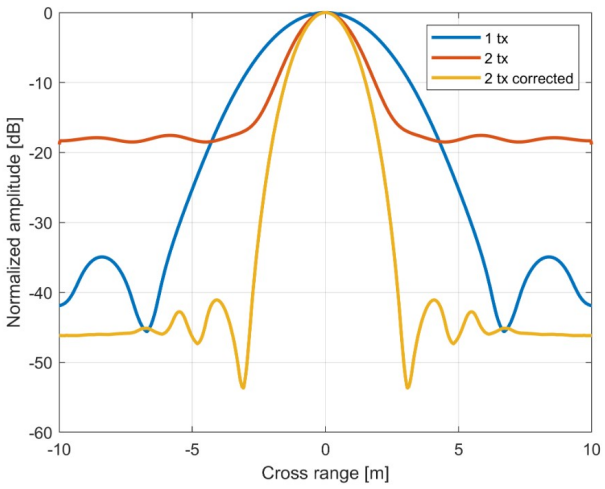

Fig. 6: Plot of the cross-range PSR of three different antenna configurations.

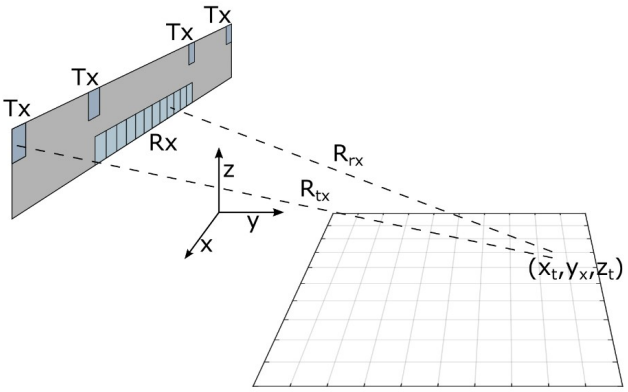

Fig. 7: Imaging geometry for the MURA-S system.

C. Antennas

Each antenna element is a crossed dipole with integrated balun, constructed using two PCBs (Printed Circuit Boards), a foam layer for mechanical strength and an Radio Frequency (RF)-transition connecting the two PCBs as shown in Fig. 8. The first PCB contains the crossed dipole. Crossing the two dipoles gives dual polarization. A bowtie shape is used to achieve the specified bandwidth. The second PCB contains the balun and the ground plane which redirects the radiated

power forward. All parts except the PCBs were produced and assembled at FFI. Identical antenna elements are used for both receive and transmit.

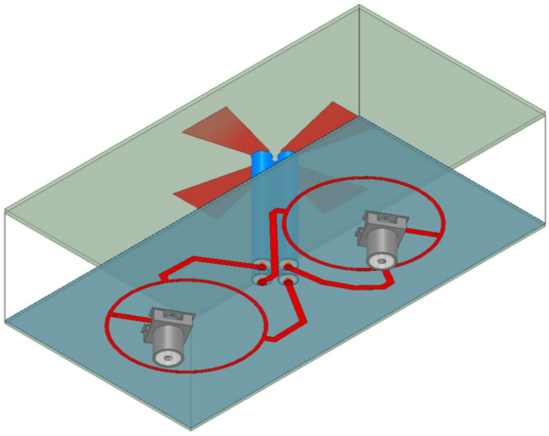

Fig. 8: A transparent 3D model of one antenna element showing the two PCBs and the RF-transition.

D. Transmitter

The transmitter mainly consists of connectorized components and evaluation boards. Fig. 9 shows a simplified block diagram of the transmitter. A Direct Digital Synthesizer (DDS) [13] is used to generate a 600–1000 MHz chirp, which is low-pass filtered and up-converted using a frequency mixer. The signal is then bandpass filtered and amplified, before it is split into Tx and LO. The Tx signal is passed to the Tx switch which selects the transmit antenna as seen in Fig. 11. The LO is used by the receiver for down-mixing.

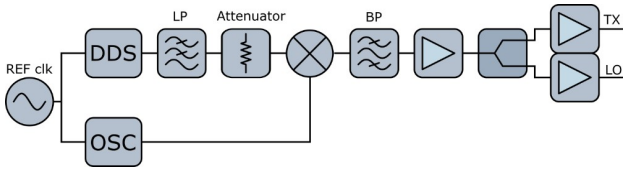

Fig. 9: A simplified block diagram of the radar transmitter.

E. Receiver

The receiver of the radar contains 16 channels, 8 for each polarization. The signal is bandpass-filtered and amplified before it is down-mixed to baseband. After down-mixing, the signal is low-pass filtered and amplified by a frequency dependent amplifier using a custom made PCB designed at FFI. The signal is then digitized using a pair of 8-channel PCI-E digitizers [14].

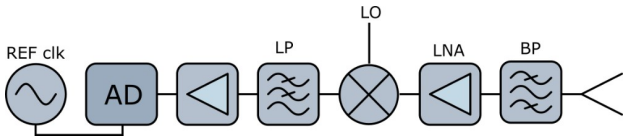

Fig. 10: A simplified block diagram of one receiving channel, some elements are omitted for brevity.

F. Control and digitization

The system is controlled from a computer containing the digitization cards. This computer communicates with the Field Programmable Gate Array (FPGA) control unit, which in turn is responsible for setting up the waveform parameters and clock distribution. The FPGA control unit also controls triggering and RF switches.

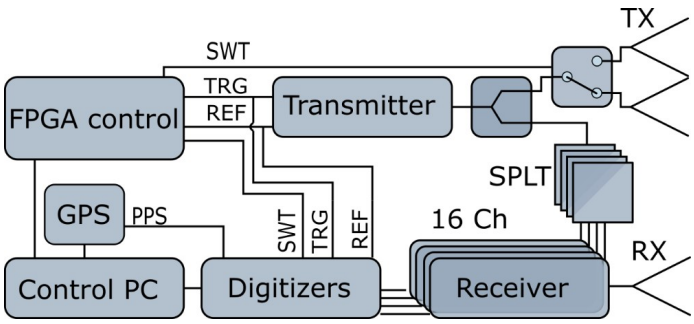

Fig. 11: A simplified block diagram of the radar systems control system.

III. Experimental results

The system was thoroughly tested to verify that the range and cross-range resolution corresponded with the simulated results and that the sidelobes in the cross-range PSR was satisfactory. The systems ability to detect obstacles without the presence of vegetation was also verified. After the successful initial testing, the system was mounted on the OLAV platform to test the system in a controlled vegetated environment as shown in Fig. 12. The ideal radar position on the vehicle would be on the roof, but this was unfortunately not achievable as it would block the view for other sensors.

Fig. 12: OLAV platform in heavy vegetation with radar mounted in front.

To test the system's ability to detect obstacles through vegetation, a test field with vegetation measuring roughly 20–50 cm of height was selected. The tests were performed by first

Dette er en postprint-versjon/This is a postprint version. Publisert versjon/Publised version: http://dx.doi.org/10.1109/RADAR.2019.8835514

driving a predefined track without obstacles present, before placing a selection of obstacles close to the path and repeating the run. The radar was setup with a pulse length of 250 μs, 400 MHz bandwidth and used all four horizontally polarized antennas transmit antennas. The obstacles included in this test were a small rock, large rock, concrete support, tree stub and a paint can as shown in Fig. 13. It is worth noting that these images are extracted from the roof-mounted camera platform, from the radars perspective the obstacles would be far more occluded.

(a) (b) (c) (d) (e)

Fig. 13: Snapshots of the obstacles from the vehicles view, taken from the daylight cameras mounted on the vehicle. From left to right, the obstacles are a small rock, large rock, concrete support, stub and a paint can respectively.

Utilizing the vehicles on-board navigation enabled us to implement radar mapping to detect the obstacles. These algorithms are currently under development, but in these initial tests time-domain backprojection, as described in by Duersch [15], was used to coherently process images from each transmit cycle. These images, formed from different vehicle locations, were in turn incoherently combined in an iterative mapping procedure. This yielded a radar map of the area as seen in Fig. 14.

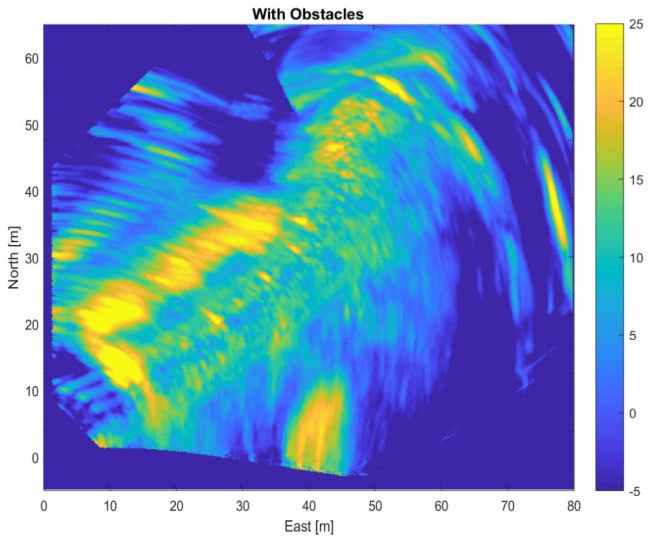

Fig. 14: Radar map of the scene with obstacles. Images are created using time-domain backprojection and mapped using the vehicles navigation and an iterative multi-look technique.

To demonstrate the obstacle detection capability a hard-threshold was set at 15 dB and an ”obstacle map” was plotted over an aerial photo as shown in Fig. 15. It is evident from Fig. 15 that the trees and metal poles close to the road are easily detected. In addition, the five obstacles are also clearly visible and separated from the surrounding clutter.

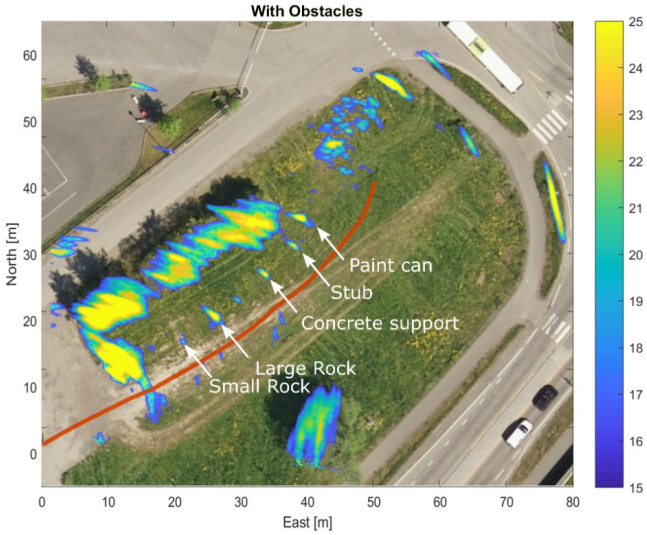

Fig. 15: Radar map of the scene with obstacles overlaid an aerial photo. A hard-threshold set at 15 dB and pixels below are set to transparent. The image clearly shows the four obstacles, as well as other potential obstacles that have not been investigated. The orange line shows the vehicles route.

To further demonstrate obstacle detection capability, the obstacle positions were compared before and after the obstacles were arranged. The resulting target signatures are imaged in Fig. 16. The figure clearly shows that the obstacles are responsible for a drastic increase in response from the respectable positions. The difference in backscattered power at the target positions is 4, 16, 11, 9 and 14 dB respectively.

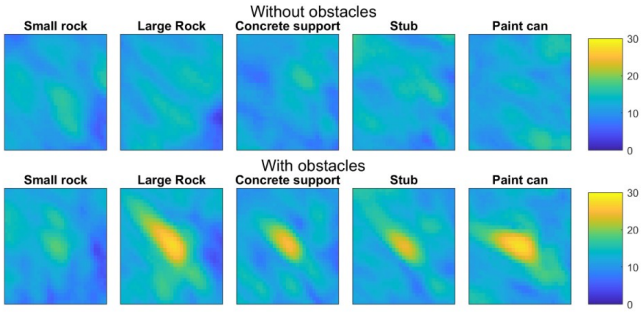

Fig. 16: A cropped part of the obstacle positions before and after obstacles were arranged.

An obstacle map created using a Velodyne HDL32 LiDAR and cameras overlaid an aerial photo is shown in Fig. 17. Comparing the obstacle map from the LiDAR with the preliminary “obstacle map” from the MURA-S it is evident they they both detect the trees. The LiDAR, however, is not able to detect the obstacles hidden in vegetation as shown by the arrows. Ideally,

Dette er en postprint-versjon/This is a postprint version. Publisert versjon/Publised version: http://dx.doi.org/10.1109/RADAR.2019.8835514

the LiDAR should detect the obstacles and the vegetation as traversable, but since it cannot the distinguish the obstacles from the vegetation it is forced to label both of them as either obstacle or traversable. In this case the algorithm has labeled them both as traversable and would be at risk of hitting an obstacle.

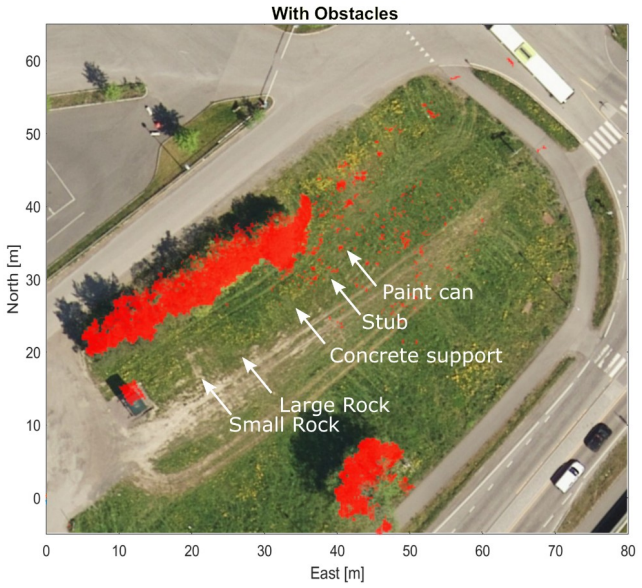

Fig. 17: Obstacle map created using a LiDAR overlaid an aerial photo and arrows pointing at the obstacle positions. It is evident that the LiDAR obstacle detection algorithm has not been able to detect the obstacles hidden in vegetation.

IV. Conclusion

The initial results from the MURA-S system are promising. It has been proven that the system is functioning, the cross-range resolution improvement due to the MIMO configuration is confirmed and the initial results indicate that the system is capable of detecting obstacles hidden in vegetation. Further work on the MURA-S system will be developing algorithms for terrain analysis, obstacle detection and classification. The system will also be tested for surveillance tasks such as UAS and personnel detection and classification.

References

[1] K. Mathiassen, M. Baksaas, L. E. Olsen, M. Thoresen, and B. Tveit, "Development of an Autonomous Off-Road Vehicle for Surveillance Missions," *NATO Science and Technology Organization.*, vol. STO-MP-IST, 2016.

[2] G. Reina, J. Underwood, G. Brooker, and H. Durrant-Whyte, "Radar-based perception for autonomous outdoor vehicles," *Journal of Field Robotics*, vol. 28, no. 6, pp. 894–913, 2011.

[3] T. Peynot, J. Underwood, and S. Scheding, "Towards reliable perception for unmanned ground vehicles in challenging conditions," *2009 IEEE/RSJ International Conference on Intelligent Robots and Systems, IROS 2009*, pp. 1170–1176, 2009.

[4] F. Ulaby and E. Wilson, "Microwave Attenuation Properties of Vegetation Canopies," *IEEE Transactions on Geoscience and Remote Sensing*, vol. GE-23, no. 5, pp. 746–753, 1985.

[5] J. Richards, "The use of multiple-polarization data in foliage penetrating (FOPEN) synthetic aperture radar (SAR) applications," *Sandia National Laboratories*, vol. SAND2002-2, 2002.

[6] M. A. Ressler, L. H. Nguyen, F. J. Koenig, and G. Smith, "Synchronous Impulse Reconstruction (SIRE) Radar Sensor for Autonomous Navigation," tech. rep., Army Research Lab Adelphi Sensors and Electron Devices Directorate.

[7] S.-G. Sun, B. Cho, G. C. Park, Y. S. Kang, and S. H. Han, "UWB forward imaging radar for an unmanned ground vehicle," pp. 1–4, 2011.

[8] B. Torvik, K. E. Olsen, and H. Griffiths, "Classification of Birds and UAVs Based on Radar Polarimetry," *IEEE Geoscience and Remote Sensing Letters*, vol. 13, no. 9, pp. 1305–1309, 2016.

[9] S. R. Cloude and E. Pettier, "A review of target decomposition theorems in radar polarimetry," *IEEE Transactions on Geoscience and Remote Sensing*, vol. 34, no. 2, pp. 498–518, 1996.

[10] G. L. Charvat, *A Low-Power Radar Imaging System*. PhD dissertation, Michigan State University, 2007.

[11] J. H. Ender and J. Klare, "System architectures and algorithms for radar imaging by MIMO-SAR," *IEEE National Radar Conference - Proceedings*, vol. 2, pp. 2–7, 2009.

[12] L. Nguyen, "Signal processing techniques for the U.S. Army Research Laboratory stepped frequency ultra-wideband radar," *Proceedings of SPIE*, vol. 10188, 2017.

[13] Analog Devices, "2.5 gsps direct digital synthesizer with 12-bit dac," *AD9915 Datasheet*, 2012.

[14] Spectrum-Instrumentation, "Spectrum M2i.4652-Exp Datasheet," 2012.

[15] M. Duersch, "Backprojection for Synthetic Aperture Radar," *All Theses and Dissertations*, pp. 1–7, 2013.